

ARCADE 2 OBSERVATIONS OF GALACTIC RADIO EMISSION

A. KOGUT¹, D. J. FIXSEN^{1,2}, S. M. LEVIN³, M. LIMON⁴, P. M. LUBIN⁵, P. MIREL^{1,6}, M. SEIFFERT⁴, J. SINGAL⁷, T. VILLELA⁸, E. WOLLACK¹, C. A. WUENSCH⁸

Draft December 15, 2008

ABSTRACT

We use absolutely calibrated data from the ARCADE 2 flight in July 2006 to model Galactic emission at frequencies 3, 8, and 10 GHz. The spatial structure in the data is consistent with a superposition of free-free and synchrotron emission. Emission with spatial morphology traced by the Haslam 408 MHz survey has spectral index $\beta_{\text{synch}} = -2.5 \pm 0.1$, with free-free emission contributing 0.10 ± 0.01 of the total Galactic plane emission in the lowest ARCADE 2 band at 3.15 GHz. We estimate the total Galactic emission toward the polar caps using either a simple plane-parallel model with $\csc(|b|)$ dependence or a model of high-latitude radio emission traced by the COBE/FIRAS map of CII emission. Both methods are consistent with a single power-law over the frequency range 22 MHz to 10 GHz, with total Galactic emission towards the north polar cap $T_{\text{Gal}} = 0.498 \pm 0.028$ K and spectral index $\beta = -2.55 \pm 0.03$ at reference frequency 1 GHz. The well calibrated ARCADE 2 maps provide a new test for spinning dust emission, based on the integrated intensity of emission from the Galactic plane instead of cross-correlations with the thermal dust spatial morphology. The Galactic plane intensity measured by ARCADE 2 is fainter than predicted by models without spinning dust, and is consistent with spinning dust contributing 0.4 ± 0.1 of the Galactic plane emission at 22 GHz.

Subject headings: radio continuum: ISM, radiation mechanisms: non-thermal, cosmic microwave background

1. INTRODUCTION

The cosmic microwave background (CMB) is a valuable probe of physical conditions in the early universe. Its frequency spectrum records the history of energy transfer between the evolving matter and radiation fields to constrain the energetics of the early universe. We view the CMB through diffuse emission from the interstellar medium. At centimeter wavelengths, the dominant contributions are from synchrotron emission originating from electrons accelerated in the Galactic magnetic field, and free-free emission (thermal bremsstrahlung) from electron-ion collisions. Thermal emission from interstellar dust is negligible, but electric dipole emission from a population of small, rapidly rotating dust grains could contribute a substantial fraction of the total Galactic emission at wavelengths near 1 cm (Draine & Lazarian 1998; Dobler & Finkbeiner 2007; Miville-Deschênes et al. 2008). Absolute measurements of the sky temperature at centimeter wavelengths measure diffuse emission to separate Galactic from primordial emission and provide information on physical processes in the interstellar medium.

The Absolute Radiometer for Cosmology, Astro-

physics, and Diffuse Emission (ARCADE) is an instrument to measure the absolute temperature of the sky in search of distortions from a blackbody spectrum. ARCADE operates at centimeter wavelengths between full-sky surveys at radio frequencies below 3 GHz and the Far Infrared Absolute Spectrophotometer (FIRAS) survey at frequencies above 60 GHz. It consists of a set of cryogenic radiometers observing at 37 km altitude from a balloon payload. Each radiometer uses a double-null design, measuring the temperature difference between a corrugated horn antenna and an internal reference as the antenna alternately views the sky or a full-aperture blackbody calibrator. The internal reference can be adjusted to null the antenna-reference signal difference, while the calibrator temperature can be independently adjusted to null the sky-calibrator signal difference. ARCADE thus measures small shifts about a precise blackbody, greatly reducing dependence on instrument calibration and stability. The calibrator, antennas, internal reference, and radiometer front-end amplifiers are mounted within a large liquid helium Dewar and are maintained near thermal equilibrium with the CMB. Boiloff helium vapor, vented through the aperture, forms a barrier between the instrument and the atmosphere to allow operation in full cryogenic mode with no windows between the optics and the sky.

A 2-channel prototype (ARCADE 1) flew in 2001 and again in 2003, observing the sky at 10 and 30 GHz to demonstrate the feasibility of cryogenic open-aperture optics (Kogut et al. 2004; Fixsen et al. 2004). A second-generation 6-channel instrument (ARCADE 2) flew in 2005 and again in 2006. A motor failure in 2005 allowed only a single channel to view the sky (Singal et al. 2006). The 2006 flight successfully obtained observations at 3.3, 8.3, 10.2, 30, and 90 GHz. Data from the 2006 flight are consistent with a blackbody CMB spec-

Electronic address: Alan.J.Kogut@nasa.gov

¹ Code 665, Goddard Space Flight Center, Greenbelt, MD 20771

² University of Maryland

³ Jet Propulsion Laboratory, California Institute of Technology, 4800 Oak Grove Drive, Pasadena, CA 91109

⁴ Columbia Astrophysics Laboratory, 550W 120th St., Mail Code 5247, New York, NY 10027-6902

⁵ University of California at Santa Barbara

⁶ Wyle Information Systems

⁷ Kavli Institute for Particle Astrophysics and Cosmology, SLAC National Accelerator Laboratory, Menlo Park, CA 94025

⁸ Instituto Nacional de Pesquisas Espaciais, Divisão de Astrofísica, Caixa Postal 515, 12245-970 - São José dos Campos, SP, Brazil

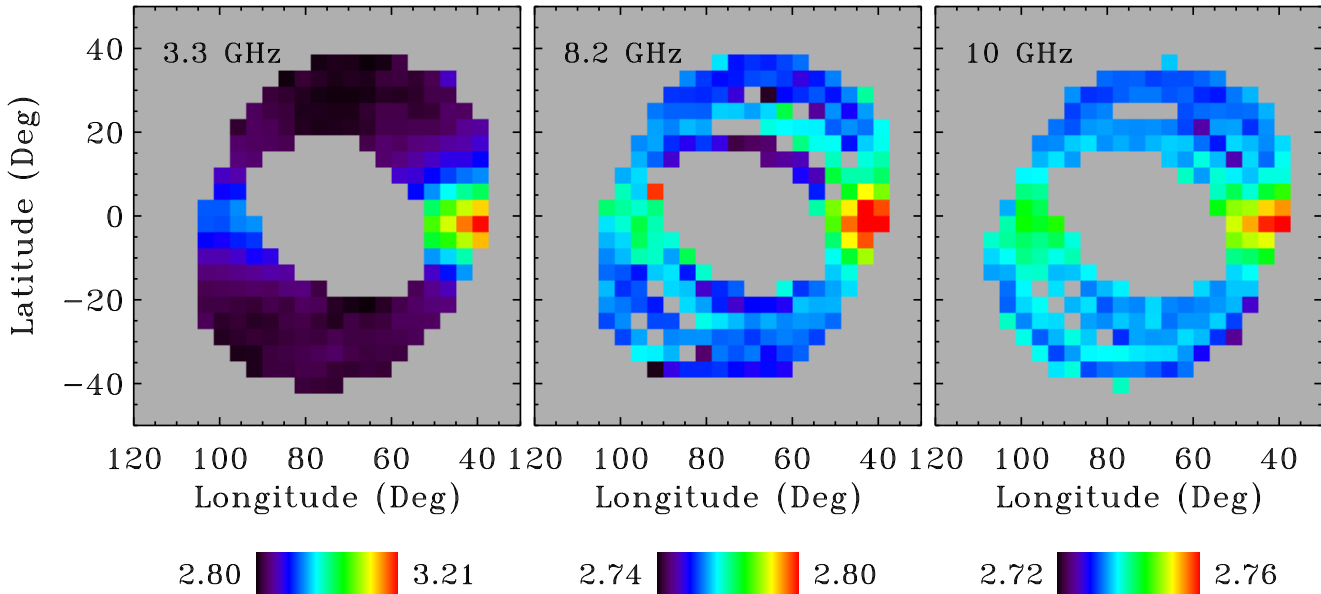


FIG. 1.— Sky maps from the ARCADE 2 2006 flight (thermodynamic temperature in Galactic coordinates). Un-observed regions are masked in grey. The Galactic plane is clearly visible.

trum, but show a clear detection of an extragalactic radio background. This paper describes the analysis of Galactic emission from the 2006 flight. Companion papers describe the ARCADE 2 instrument (Singal et al. 2008), the calibration and sky temperature analysis (Fixsen et al. 2008) and the implications of the detected extra-Galactic radio background (Seiffert et al. 2008).

2. OBSERVATIONS AND SKY MAPS

The ARCADE 2 instrument launched from the Columbia Scientific Balloon Facility in Palestine, TX carrying a complement of 7 Dicke-switched radiometers and 1800 liters of liquid helium. During ascent, the Dicke switch failed in one radiometer. The remaining radiometers began sky observations on 2006 July 22 at 05:08 UT, continuing through 08:11 UT just prior to flight termination.

Figure 1 shows the absolute sky temperatures binned by Galactic coordinates. Each radiometer views the sky through a corrugated conical feed horn, scaled with wavelength to produce a Gaussian beam with 11.6° full width at half maximum (Singal et al. 2005). The beams point 30° from the zenith and the entire payload spins at 0.6 RPM so that the beams scan a circle of 60° diameter centered on the zenith. The spin frequency is comparable to the $1/f$ knee of the instrument noise, so that strip-

ing at the mK level is visible in the binned data. Each radiometer observed roughly 7% of the sky.

The measured sky temperatures are dominated by the CMB monopole. Galactic emission is clearly visible in the data at 3, 8, and 10 GHz. At higher frequencies, the smaller Galactic signal and higher instrument noise combine to prevent a clear detection of Galactic emission. Throughout this paper, we consider only data from the 3, 8, and 10 GHz radiometers. Table 1 summarizes the in-flight performance of each radiometer. We compute the instrument noise by comparing the variance of the data within each sky bin to the number of observations in that bin. This value for the noise thus includes calibration as well as the effect of low-frequency striping.

TABLE 1
FREQUENCY BANDS FOR FOREGROUND ANALYSIS

| Frequency (GHz) | Bandwidth (MHz) | White Noise $\text{mK s}^{1/2}$ |
|--------------------|--------------------|------------------------------------|
| 3.15 | 210 | 11.8 |
| 3.41 | 220 | 10.1 |
| 7.98 | 350 | 5.5 |
| 8.33 | 350 | 5.2 |
| 9.72 | 860 | 3.0 |
| 10.49 | 860 | 3.0 |

The observed emission is a combination of CMB, synchrotron, and free-free emission. Synchrotron emission results from the acceleration of cosmic ray electrons in the Galactic magnetic field. For a power-law distribution of electron energies $N(E) \propto E^{-p}$ propagating in a uniform magnetic field, the synchrotron emission is also a power law,

$$T_A(\nu) \propto \nu^{-\beta_s} \quad (1)$$

where T_A is antenna temperature, ν is the radiation frequency, and $\beta_s = -(p + 3)/2$ (Rybicki & Lightman 1979). Free-free emission is also a power law in antenna temperature, with spectral index $\beta_{\text{ff}} = -2.15$.

We evaluate the observed spectral index in the ARCADE 2 sky maps by plotting the temperature observed at one frequency against the temperature of the same sky pixel observed at a different frequency. Since the ARCADE 2 absolute calibration is derived from comparison of sky data to a blackbody calibrator of known physical temperature, the sky solutions have units of thermodynamic temperature (Fixsen et al. 2008). In order to evaluate the spectral index, we convert the sky maps (Fig. 1) from thermodynamic to antenna temperature

$$T_A = \frac{x}{\exp(x) - 1} T \quad (2)$$

where T is thermodynamic temperature, $x = h\nu/kT$, h is Planck's constant, and k is Boltzmann's constant. Figure 2 shows the resulting TT plots.

The same Galactic features are observed at each frequency. A linear fit to each plot yields spectral index $\beta = -2.43 \pm 0.03$ from 3.3 to 8.3 GHz, $\beta = -2.47 \pm 0.02$ from 3.3 to 10.3 GHz, and $\beta = -3.12 \pm 0.17$ from 8.3 to 10.3 GHz, where the quoted errors include the measurement uncertainties in both maps for each plot. The measured index is consistent with a superposition of synchrotron and free-free emission.

3. SPATIAL STRUCTURE

A search for distortions in the CMB spectrum requires correction of Galactic foreground emission. The ARCADE 2 data has only six frequency channels containing significant Galactic emission (Table 1), and can not uniquely separate the observed emission into individual components (synchrotron, free-free, or other sources). We combine the ARCADE 2 data with other sky surveys in order to model foreground emission.

A widely-used technique describes the observed emission at each frequency ν as a linear combination of fixed “template” maps,

$$T_A(\nu, p) = \sum_i \alpha_i(\nu) G_i(p) \quad (3)$$

where p is a pixel index and $G_i(p)$ are a set of sky maps tracing different components of the interstellar medium. The spectral dependence of the fitted coefficients $\alpha(\nu)$ can then be ascribed to the component traced by each template.

Several choices for template maps tracing free-free emission are available. Gold et al. (2008) use a maximum-entropy algorithm to derive a map of free-free emission based on the Wilkinson Microwave Anisotropy Probe (WMAP) 5-year data and a compilation of H α

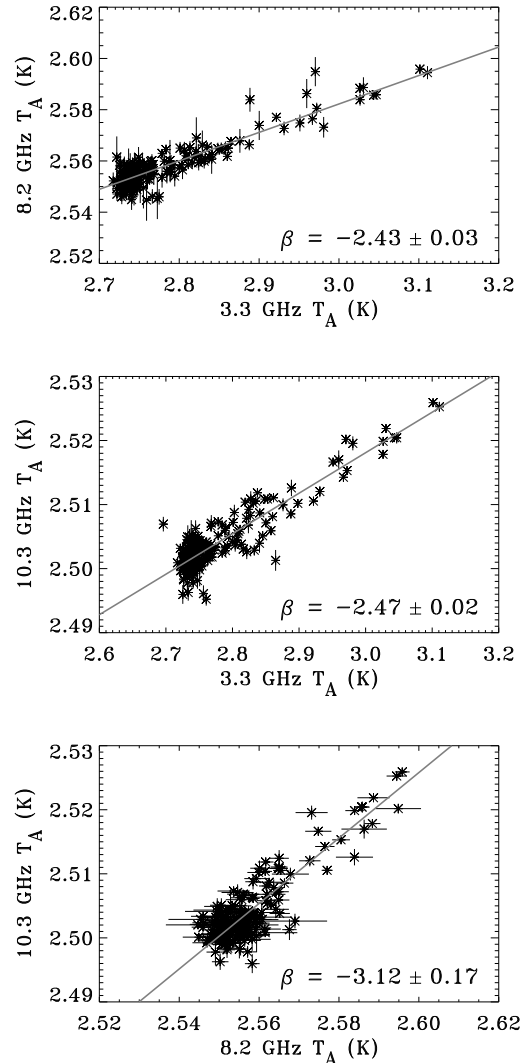


FIG. 2.— TT plots from the ARCADE 2 sky maps in units of antenna temperature. The best-fit spectral index (solid line) is consistent with a superposition of synchrotron and free-free emission.

emission (Finkbeiner 2003). Since the maximum-entropy method (MEM) template is heavily weighted by the microwave data in the Galactic plane, it minimizes extinction effects in the H α map. As alternatives to the maximum-entropy template, we also use either a map of thermal dust emission (Finkbeiner, Davis, & Schlegel (1999) model 8) or the FIRAS map of CII emission at 158 μm (Fixsen, Bennett, & Mather 1999), neither of which is affected by extinction.

The choice of synchrotron template depends on the treatment of spatial variation in the synchrotron spectral index. To the extent that this variation can be neglected, the 408 MHz survey (Haslam et al. 1981) provides a high signal-to-noise ratio tracer for synchrotron emission. Since the 408 MHz survey contains both free-free and synchrotron emission, we correct it for free-free emission using the MEM free-free template scaled to 408 MHz using a spectral index $\beta_{\text{ff}} = -2.15$ so that to first order the template represents only synchrotron emission. We convolve both the synchrotron and free-free templates to

TABLE 2
COEFFICIENTS FOR SPATIAL TEMPLATES

| Frequency (GHz) | α_{ff} (mK nW ⁻¹ m ² sr) | α_s (mK/K) |
|--------------------|---|----------------------|
| 3.15 | 3.22 ± 0.11 | 2.02 ± 0.05 |
| 3.41 | 3.06 ± 0.09 | 1.70 ± 0.04 |
| 7.98 | 0.26 ± 0.05 | 0.24 ± 0.02 |
| 8.33 | 0.28 ± 0.05 | 0.24 ± 0.02 |
| 9.72 | 0.39 ± 0.03 | 0.04 ± 0.01 |
| 10.49 | 0.37 ± 0.03 | 0.05 ± 0.01 |

match the ARCADE 11°6' beam width.

The ARCADE 2 data are dominated by the CMB monopole, even towards the Galactic plane. Both the Galactic and extragalactic signals also contain monopole terms, as do the synchrotron and free-free templates. We thus include a monopole template as a nuisance parameter and compute the template coefficients $\alpha_i(\nu)$ by minimizing

$$\chi^2 = \sum_p \frac{[T_A(p, \nu) - \alpha_0(\nu) - \alpha_{\text{ff}}(\nu)G_{\text{ff}}(p) - \alpha_s(\nu)G_s(p)]^2}{\sigma(p, \nu)^2} \quad (4)$$

where α_0 , α_{ff} , and α_s are the coefficients for the monopole, free-free, and synchrotron templates, respectively, and $\sigma(p, \nu)$ is the instrument noise in each pixel and frequency channel.

The spatial structure in the ARCADE 2 data may be described as a superposition of emission traced by the Haslam 408 MHz survey and the FIRAS map of CII emission. Table 2 shows the fitted coefficients for the best-fit template combination. Fitting the coefficients from each template to a power law in frequency yields spectral indices -2.5 ± 0.1 for emission traced by the 408 MHz survey and -2.0 ± 0.1 for emission traced by the CII map.

The best template model uses the 408 MHz survey to trace synchrotron emission and the FIRAS map of CII line emission to trace free-free emission. We have repeated the template fits using different tracers for synchrotron or free-free emission, obtaining broadly similar results. In all cases, the best choice for free-free template is either the CII map or the thermal dust map. We note that spatial structure in the ARCADE 2 maps is dominated by the Galactic plane, where extinction corrections for free-free maps derived from H α emission are worst. The ratio of emission traced by the CII free-free template to emission traced by the 408 MHz synchrotron template is $\langle T_{\text{ff}}/T_{\text{synch}} \rangle = 0.16 \pm 0.01$ evaluated for latitudes $|b| < 10^\circ$ in the lowest ARCADE 2 channel at 3.15 GHz. The ratio of free-free emission to the total Galactic plane emission is $\langle T_{\text{ff}}/T_{\text{total}} \rangle = 0.10 \pm 0.01$.

4. GALACTIC POLAR CAP TEMPERATURE

The sky temperature measured by ARCADE 2 includes contributions from Galactic, extragalactic, and cosmic sources. The 2.7 K cosmic microwave background dominates the measured temperatures. Galactic emission is dominated by synchrotron emission, with a smaller contribution from free-free sources. The integrated contribution of similar synchrotron and free-free emission in external galaxies constitutes an isotropic extragalactic radio background. Accurate measurement of the extragalactic or cosmic backgrounds requires reliable determination of both the spatial structure and the zero

level of the Galactic emission.

Although the cosmic microwave background may be distinguished from Galactic or extragalactic radio emission by the different frequency dependences, spectral fitting alone can not distinguish Galactic emission from an extragalactic component of similar spectral behavior. The template model above reproduces the spatial structure of the observed Galactic emission, but is insensitive to emission described by an additive constant in each map. If the total Galactic brightness were determined along some fiducial line of sight, we could add a monopole term to the template model to match the total Galactic brightness along that line of sight. The adjusted model would then characterize Galactic emission along all other lines of sight.

The north and south polar caps (latitude $|b| > 75^\circ$) provide convenient reference lines of sight. We use two independent methods to estimate the total Galactic emission toward the Galactic polar caps. The first method relies solely on the spatial morphology, assuming a plane-parallel model to estimate the total Galactic emission at the polar caps. A second, independent method compares the spatial morphology of the ARCADE 2 and other radio maps to template maps of atomic line emission in order to estimate the amount of radio emission per unit line emission. Since line emission can unambiguously be attributed to the Galaxy, the total Galactic radio emission toward the polar caps may then be estimated by

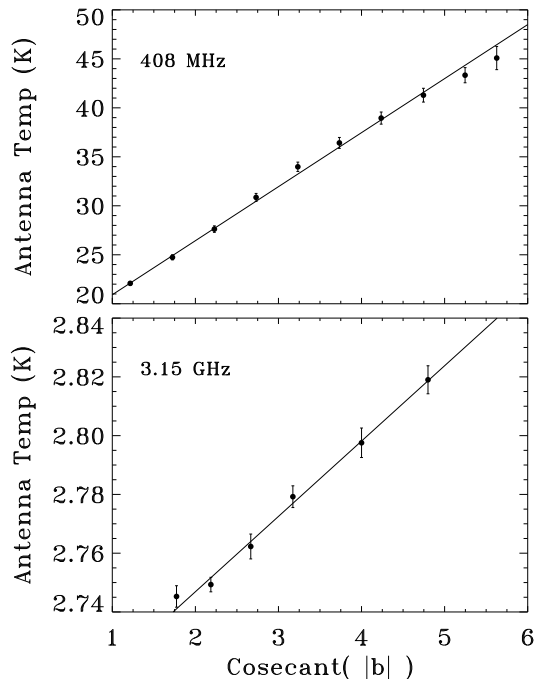


FIG. 3.— Temperature of the 408 MHz survey (top) and ARCADE 3.15 GHz channel (bottom) binned by $\text{csc}(b)$ for latitudes $b > 10^\circ$ (Northern hemisphere). Sky temperatures include the CMB and any extragalactic background. The scatter about the best-fit line results from the higher-order spatial structure in the maps. For clarity, the plotted uncertainties have been inflated by a factor of 20 (408 MHz survey) or 5 (ARCADE); the actual statistical uncertainties for the mean of each bin are smaller than the symbol size. The data are consistent with a plane-parallel model whose measured slope provides an estimate of the Galactic emission at the poles.

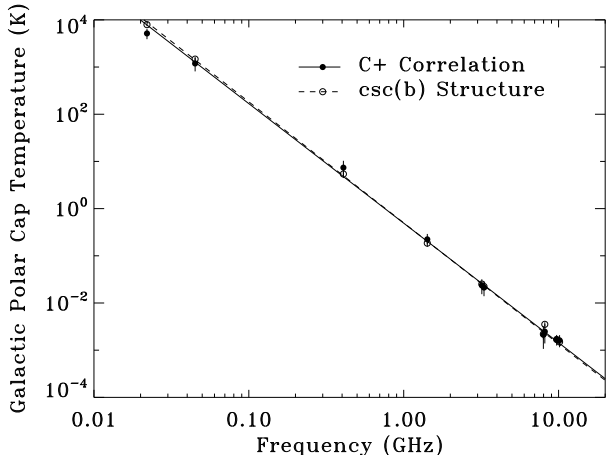


FIG. 4.— Galactic emission $T_G(\nu)$ towards the North galactic pole, derived from a cosecant fit to the spatial structure (open circles) and the radio/CII correlation (filled circles). Both methods agree and are consistent with a single power law over the frequency range 22 MHz to 10 GHz. The fitted Galactic temperature towards the polar caps can be combined with the template model of the spatial structure to fully specify the Galactic model.

scaling the total line emission at the caps by the observed ratio of radio to line emission. Both methods yield similar values for the total Galactic emission in the polar cap regions.

4.1. Polar Cap Temperature From $\text{csc}(b)$

A commonly used method to estimate total Galactic brightness models the Galaxy as a simple plane-parallel structure and fits the spatial distribution of the radio continuum at Galactic latitude $|b| > 10^\circ$ to the form

$$T_A(\nu, p) = c(\nu) + T_G(\nu) \text{csc}(|b|) \quad (5)$$

where b is the Galactic latitude of each pixel p and the constant $c(\nu)$ accounts for the contribution from the CMB or extragalactic backgrounds at each frequency ν . Figure 3 shows typical results for the northern hemisphere, both for the lowest frequency ARCADE 2 channel and the 408 MHz survey. The high-latitude structure of the radio sky is consistent with a plane-parallel model, whose slope defines the antenna temperature $T_G(\nu)$ of Galactic emission toward the Galactic poles.

We repeat the cosecant fit (Eq. 5) independently for the northern and southern hemispheres, using each of the ARCADE 2 sky maps as well as a selection of lower-frequency radio surveys. Surveys at 22 MHz (Roger et al. 1999), 45 MHz (Maeda et al. 1999; Alvarez et al. 1997), 408 MHz (Haslam et al. 1981), and 1420 MHz (Reich, Testori, & Reich 2001; Reich & Reich 1986) have full or nearly full sky coverage at frequencies where the sky brightness is dominated by Galactic radio emission. For each sky map, we compute the cosecant slope $T_G(\nu)$ and its uncertainty, including both statistical and calibration uncertainties. Although the binned data are broadly consistent with a plane-parallel model, higher-order structure causes the binned data to show greater scatter about the best-fit slope than would be expected given the formal statistical uncertainty in the mean of each bin. We account for higher-order structure by inflating the statistical uncertainty to force χ^2 to unity per degree of freedom about

the best-fit line. We then add the calibration uncertainty (of order 10% for the low-frequency radio surveys) in quadrature with the (inflated) statistical uncertainty to derive the total uncertainty in the cosecant slope for each sky survey.

Figure 4 shows the Galactic temperature $T_G(\nu)$ towards the north polar cap derived from the spatial morphology of the maps. Although the sky has significant longitudinal substructure within each latitude bin, the binned data for each map strongly supports the gross morphology dominated by a plane-parallel structure. The derived polar cap temperature is consistent with a single power law over the frequency range 22 MHz to 10 GHz.

4.2. Radio/CII Correlation

Maps of line emission provide a valuable tracer of Galactic emission. Line emission from the diffuse interstellar medium can be measured over the full sky, has a well-defined amplitude along every line of sight, and does not suffer from extragalactic contamination. Several lines could be used to trace Galactic microwave emission. $\text{H}\alpha$ emission from 3–2 transition in neutral atomic hydrogen has been mapped over the full sky and is a well-established tracer of free-free emission. However, $\text{H}\alpha$ emission predominantly traces emission from the warm ionized medium, and may not accurately trace emission from the brighter synchrotron component. In addition, $\text{H}\alpha$ emission suffers from dust extinction in the Galactic plane making it less reliable in regions where the Galactic radio emission is brightest. The 21 cm fine-structure line from neutral hydrogen has also been mapped over the full sky. However, since HI emission originates from the neutral component of the interstellar medium, it is unlikely to trace microwave emission from ionized regions. The CII line at 158 μm wavelength from singly ionized carbon can be used to trace diffuse radio emission. It is optically thin even in the plane, does not suffer from dust extinction, and is an important cooling mechanism for the diffuse interstellar medium. It has been

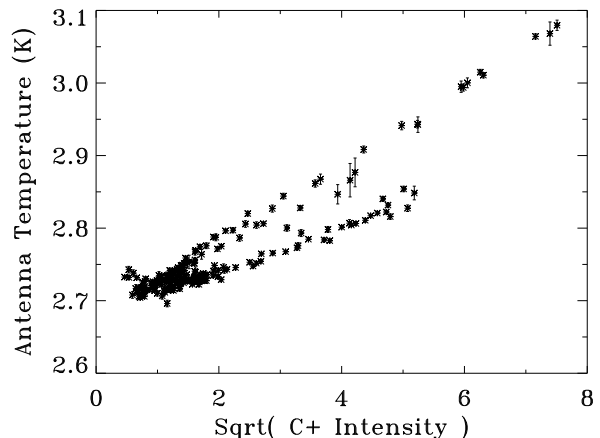


FIG. 5.— Correlation between the ARCADE 3.15 GHz intensity and the CII 158 μm atomic line in units $\text{nW m}^{-2} \text{sr}^{-1}$. The data clearly divide into two regions each with radio intensity proportional to the square root of the CII intensity. The upper track originates from pixels near the Galactic center, while the lower track originates from pixels near the Cygnus region.

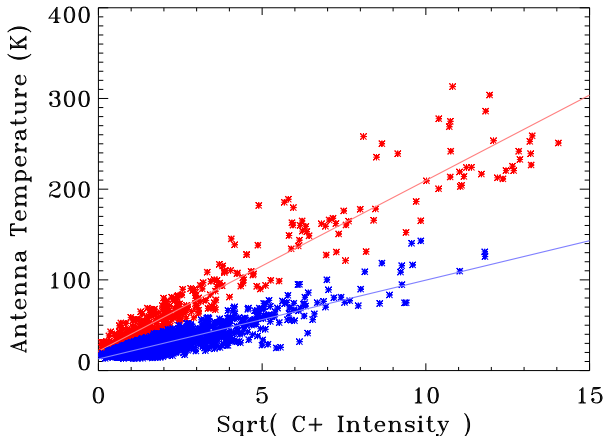


FIG. 6.— Correlation between the full-sky 408 MHz survey and the CII 158 μm atomic line in units $\text{nW m}^{-2} \text{sr}^{-1}$. The bifurcation observed in the limited ARCADE 2 sky coverage persists over larger regions of the sky. We fit the data to two lines and iteratively assign each point to one line or the other (see text for details). Colors indicate the final assignments.

mapped over the full sky by the COBE/FIRAS instrument (Fixsen, Bennett, & Mather 1999).

Figure 5 shows the correlation between the ARCADE 3.15 GHz map and the CII 158 μm map. The CII map has been smoothed to angular resolution $11'6''$ to match the ARCADE resolution. The data segregate into two tracks, an upper track from emission near the Galactic center and a lower track from emission near the Cygnus region. Both tracks show radio emission proportional to the square root of the CII intensity. This would be expected if the radio emission were proportional to the density n in the interstellar medium (e.g. from synchrotron emission), while the collisionally excited CII intensity were proportional to n^2 . Microwave free-free emission, proportional to n^2 , would result in a curved track in Figure 5. The absence of any such curvature provides additional evidence that free-free emission is faint compared to synchrotron at the ARCADE 2 bands. Note, though, that if a separate template is provided for the synchrotron component, the CII map may be used to trace the fainter free-free component (at least at the ARCADE angular resolution).

The prominent segregation in Fig 5 results at least in part from the limited sky coverage. The brightest regions in the ARCADE 2 maps occur at the edge of the Galactic center region and again at the edge of the Cygnus region. The ratio of CII intensity to the far-infrared continuum is known to differ by a factor of two between these regions (Fixsen, Bennett, & Mather 1999). We investigate the extent to which the ratio of CII intensity to radio continuum emission varies by performing a similar analysis on radio surveys at 22 , 45, 408, and 1420 MHz. All exhibit evidence for similar segregation, although not as pronounced as for the smaller ARCADE 2 sky coverage.

Figure 6 shows the correlation between the CII map and the 408 MHz survey, after smoothing the 408 MHz survey with a 5° FWHM Gaussian to approximate the 7° tophat FIRAS beam. We quantify the tendency for the data to segregate into two tracks by fitting two lines to the correlation plot. After a first guess at the fit pa-

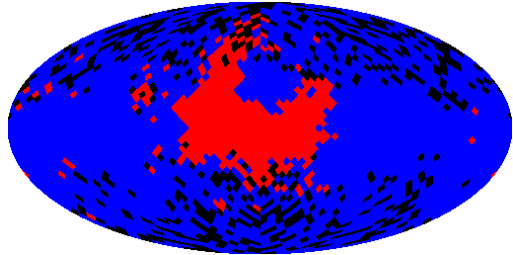


FIG. 7.— Pixel masks in Galactic coordinates showing the location of emission components from Fig. 6. Pixels with higher radio/CII correlation (red) lie near the Galactic center or along the North Galactic spur (radio Loop I). Pixels in blue have radio/CII correlation smaller by a factor of roughly 2. Pixels in black have poor signal to noise ratio in the CII map and are not used.

rameters (intercept and slope for each line), we assign each point to one line or the other based on the difference in antenna temperature between that point and either line. We then re-compute the fit parameters for each line using only those points assigned to that line, and then re-assign all points based on the new fit parameters. Several iterations suffice to produce a stable solution independent of the initial guess. The segregation is statistically significant: fitting the 2538 points to two lines reduces the χ^2 by a factor of 4 compared to a single line fit to all points.

The segregation in the correlation plot can be related to known structures in the radio sky. The points in Fig. 6 are colored to highlight the segregation into two components. Figure 7 maps each point in Galactic coordinates. Points associated with higher radio/CII ratio lie toward the Galactic center and the North Galactic Spur (radio Loop I). Both are regions with enhanced synchrotron emission.

4.3. Polar Cap Temperature From CII Correlation

The observed correlation between radio emission and CII intensity allows a well-defined determination of the associated Galactic radio emission toward the Galactic poles. We use the pixel masks defined by the 408 MHz/CII correlation (Figure 7) to fit each radio survey to the form

$$T_A(\nu, p) = \sum_{i=1}^2 b_i(\nu) + a_i(\nu) (I_C(p))^{0.5}, \quad (6)$$

where T_A is the antenna temperature at frequency ν , I_C is the CII intensity, and p denotes the pixels within one of the two spatial masks.

The intercepts b_i for the two masks include contributions from extragalactic sources (including, notably, the CMB monopole) and can not uniquely determine absolute level of Galactic emission. We instead define the Galactic emission at the polar caps by extrapolating the observed radio/CII correlation to high latitude:

$$T_G(\nu) = a(\nu) I_{\text{cap}}^{0.5}, \quad (7)$$

TABLE 3
RADIO/CII CORRELATION SLOPE

| Frequency (GHz) | Correlation Slope a (mK [nW m ⁻² sr ⁻¹] ^{-0.5}) | | |
|--------------------|---|----------------------------------|----------------------------------|
| | Mask 1 | Mask 2 | Mean |
| 0.022 | $(1.12 \pm 0.06) \times 10^4$ | $(0.74 \pm 0.02) \times 10^4$ | $(0.93 \pm 0.19) \times 10^4$ |
| 0.046 | $(2.74 \pm 0.07) \times 10^3$ | $(1.56 \pm 0.03) \times 10^3$ | $(2.15 \pm 0.63) \times 10^3$ |
| 0.408 | 18.1 ± 0.3 | 8.5 ± 0.1 | 13.3 ± 5.0 |
| 1.420 | $(5.11 \pm 0.08) \times 10^{-1}$ | $(2.94 \pm 0.04) \times 10^{-1}$ | $(4.02 \pm 1.10) \times 10^{-1}$ |
| 3.195 | $(5.63 \pm 0.12) \times 10^{-2}$ | $(2.88 \pm 0.09) \times 10^{-2}$ | $(4.25 \pm 1.38) \times 10^{-2}$ |
| 3.300 | $(5.05 \pm 0.11) \times 10^{-2}$ | $(2.61 \pm 0.08) \times 10^{-2}$ | $(3.82 \pm 1.20) \times 10^{-2}$ |
| 8.15 | $(5.73 \pm 0.37) \times 10^{-3}$ | $(1.99 \pm 0.36) \times 10^{-3}$ | $(3.86 \pm 1.87) \times 10^{-3}$ |
| 8.33 | $(6.32 \pm 0.34) \times 10^{-3}$ | $(2.59 \pm 0.26) \times 10^{-3}$ | $(4.46 \pm 1.86) \times 10^{-3}$ |
| 9.72 | $(3.68 \pm 0.15) \times 10^{-3}$ | $(2.37 \pm 0.16) \times 10^{-3}$ | $(3.03 \pm 0.66) \times 10^{-3}$ |
| 10.15 | $(3.67 \pm 0.16) \times 10^{-3}$ | $(2.17 \pm 0.18) \times 10^{-3}$ | $(2.92 \pm 0.75) \times 10^{-3}$ |

where I_{cap} is the mean intensity of the CII map at the polar caps (Galactic latitude $|b| > 75^\circ$).

The two spatial masks separate the sky into regions with higher or lower radio emission per unit CII intensity. The difference between these two components is less clear at high latitude where both the radio emission and CII intensity become weaker. The spatial segregation of the two components suggests that the south polar cap region is associated with the weaker radio/CII component (Figure 7). The brighter radio regions associated with the North Galactic spur, however, extend to high latitude so that the mean radio brightness associated with CII emission toward the north polar cap region probably lies between the limiting cases established by the two masks. We therefore use the mean of the slopes from the two masks to estimate the Galactic radio emission at the north polar cap, with uncertainty broad enough to bracket the two cases. The mean value thus derived is consistent with similar analysis fitting a single slope to the full sky. Within the restricted ARCADE 2 sky coverage, however, the value of a single slope fitted to the entire observed region could vary significantly as the sky coverage shifts slightly to include more or less of the Galactic center region. The mean of the two observed slopes is less susceptible to variations in the ARCADE 2 sky coverage.

Table 3 shows the correlation slopes $a_i(\nu)$ fitted to each mask for both the ARCADE 2 data and lower-frequency sky surveys. Figure 4 compares the Galactic temperature towards the north polar cap, derived from mean CII correlation, to the value derived from the cosecant fit. Both methods provide similar estimates for the Galactic component of the total brightness temperature towards the north polar cap. This Galactic component is consistent with a single power law

$$T_G(\nu) = T_{\text{Gal}}(\nu/\nu_0)^\beta \quad (8)$$

with spectral index $\beta = -2.55 \pm 0.03$ and amplitude $T_{\text{Gal}} = 0.498 \pm 0.028$ K at reference frequency $\nu_0 = 1$ GHz.

The analysis above uses a single map (CII line emission) to trace Galactic emission from the diffuse interstellar medium. If a significant fraction of Galactic radio emission originated from a component of the interstellar medium not well sampled by CII emission, the resulting correlation would under-estimate the total Galactic emission toward the polar cap. We test for additional microwave emission from other components of the interstellar medium by repeating the correlation analy-

sis using a simultaneous fit to three line maps chosen to sample different components of the diffuse interstellar medium: the (square root of the) COBE/FIRAS map of CII emission, a map of H α emission (Finkbeiner 2003), and the Leiden/Argentine/Bonn Galactic HI Survey (Kalberla et al. 2005). The simultaneous fit produces results nearly identical to a fit using just the CII map, shifting the derived Galactic polar cap temperature by 11 ± 21 mK at reference frequency 1 GHz. Since the limited ARCADE 2 sky coverage increases the effect of covariance between the different line maps, we use the results derived from the single CII correlation.

4.4. Composite Galactic Model

Removing Galactic emission from the ARCADE 2 data requires a model for both the spatial structure and the total Galactic emission. At each ARCADE frequency, we generate a full-sky model of the spatial structure using full-sky template maps multiplied by the coefficients fitted within the region observed by ARCADE 2 (Table 2). We then add a constant to the template model to match the total Galactic emission derived from the CII and $\text{csc}(|b|)$ fits towards selected reference positions.

We independently model the total Galactic emission toward the north and south Galactic polar caps ($|b| > 75^\circ$). For each reference position, we compute the total Galactic emission associated with either the plane-parallel structure (Eq. 5) or the CII emission (Eq. 7). We apply each method to the ARCADE 2 and radio surveys, and parameterize the resulting multi-frequency results using a power-law model (Eq. 8). As a cross-check, we also estimate the total Galactic emission for the coldest patch in the Northern hemisphere, consisting of all pixels within 15° of $b = 48^\circ$, $l = 196^\circ$ (north of the Galactic anti-center). Since by definition a mid-latitude cold spot is inconsistent with a plane-parallel structure, the estimate for this position is based only on the radio/CII correlation. Table 4 shows the estimated Galactic normalization T_{Gal} and spectral index β for each reference position. We obtain similar results using either the spatial morphology or the radio/CII correlation.

We fix the offset of the template model (Eq. 3) by computing the temperature of the template model towards these same regions, then adding a constant $\alpha_0(\nu)$ to the template model at each frequency ν to force the template model to match the power-law model along these lines of sight. The resulting composite model of Galactic emission can be used to correct the calibrated time-ordered data in order to estimate the CMB

TABLE 4
GALACTIC EMISSION^a ALONG SELECTED LINES OF SIGHT

| Parameter | Technique | North Polar Cap | South Polar Cap | Coldest Patch |
|----------------------|---------------|-------------------|-------------------|-------------------|
| T_{Gal} (K) | Radio/CII | 0.492 ± 0.095 | 0.303 ± 0.054 | 0.188 ± 0.130 |
| | csc($ b $) | 0.499 ± 0.030 | 0.366 ± 0.028 | — |
| | Weighted Mean | 0.498 ± 0.028 | 0.353 ± 0.025 | 0.188 ± 0.130 |
| β | Radio/CII | -2.53 ± 0.07 | -2.59 ± 0.06 | -2.56 ± 0.12 |
| | csc($ b $) | -2.56 ± 0.04 | -2.65 ± 0.05 | — |
| | Weighted Mean | -2.55 ± 0.03 | -2.63 ± 0.04 | -2.56 ± 0.12 |

^a Galactic emission $T_G(\nu) = T_{\text{Gal}}(\nu/\nu_0)^\beta$ with reference frequency $\nu_0 = 1$ GHz.

monopole temperature and the extragalactic radio background (Fixsen et al. 2008). The offsets derived from the three independent regions agree within 5 mK at 3 GHz, which we adopt as the uncertainty in the zero level of composite Galactic model.

The spectral index derived for the Galactic emission toward the polar caps or coldest region, $\beta \approx -2.57 \pm 0.03$, is consistent with the spectral index $\beta = -2.5 \pm 0.1$ derived from the synchrotron template fit only to ARCADE 2 data, indicating that high-latitude Galactic emission is dominated by synchrotron emission at frequencies below 10 GHz. A synchrotron spectral index of -2.57 is significantly flatter than the values derived from measurements at higher frequencies, but is consistent with the majority of measurements below 10 GHz (see, e.g., the tabulation in Rogers & Bowman (2008)). Notable exceptions are the measurements by Tartari et al. (2008) and Platania et al. (1998), which prefer $\beta \approx -2.8$ for the synchrotron component. Both of these results are derived from a single strip at declination $\delta = +42^\circ$ and may not be representative of larger regions of the sky.

5. SPINNING DUST

The ARCADE 2 data can also be used to search for additional microwave emission associated with interstellar dust. The microwave sky is known to contain a component spatially correlated with far-infrared dust emission but not with synchrotron-dominated surveys at 408 or 1420 MHz (Kogut et al. 1996a,b; de Oliveira-Costa et al. 1997; Leitch et al. 1997; Bennett et al. 2003). The frequency spectrum of the correlated component differs markedly from the emission spectrum of thermal dust, showing a spectral index $\beta \approx -2.2$ in antenna temperature from 20 to 50 GHz.

Two main candidates have emerged to explain this “anomalous” correlated emission component. Electric dipole emission from a population of small, rapidly rotating dust grains will produce a spectrum with a broad peak in the frequency range 20–40 GHz (Draine & Lazarian 1998). Miville-Deschênes et al. (2008) analyze data from the Wilkinson Microwave Anisotropy Probe (WMAP) mission and conclude that spinning dust accounts for the majority of emission in the Galactic plane at 22 GHz. An alternative model explains the correlated emission as flat-spectrum synchrotron emission associated with star formation activity (Bennett et al. 2003; Gold et al. 2008). Energy losses as electrons propagate from their origin steepen the synchrotron index away from these sources. Since a flat-spectrum component will increasingly dominate at higher frequencies, the spatial morphology of synchrotron emission at higher frequencies should increasingly resemble

thermal dust emission from the same star formation activity.

Efforts to distinguish between these models have largely focused on the frequency spectrum of the dust-correlated component inferred by correlating a map tracing thermal dust emission against microwave maps at different observing frequencies. The correlation with thermal dust emission is seen to peak at frequencies between 20 and 30 GHz, falling at frequencies below 22 GHz (de Oliveira-Costa et al. 2004; Fernández-Cerezo et al. 2006; Hildebrandt et al. 2007). This falling spectrum at low frequencies has been cited as evidence favoring spinning dust models.

The decrease in dust-correlated emission at frequencies below 20 GHz, although consistent with spinning dust emission, does not necessarily support such models over the flat-spectrum synchrotron alternative. *Both* models predict weaker correlation with thermal dust emission at frequencies below 20 GHz. For the spinning dust model, the weaker correlation results from the lower amplitude of the spinning dust emission. The flat-spectrum synchrotron model, however, also predicts a weaker correlation at lower frequencies, since by construction the spatial morphology of the sky in this model varies smoothly from the WMAP data at 22 GHz (observed to correlate

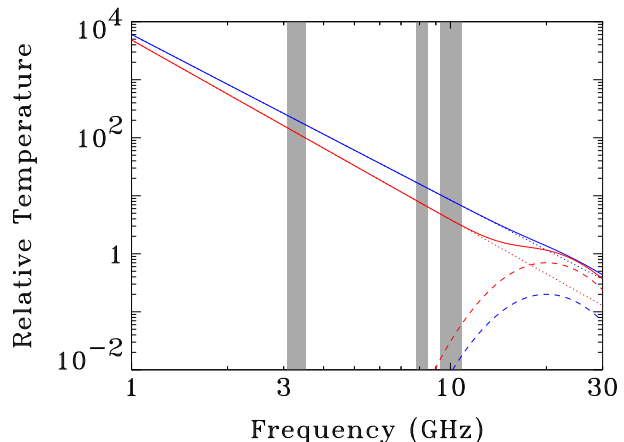


FIG. 8.— Synchrotron and spinning dust emission for two models with different spinning dust amplitude. The red (blue) curves show emission from a model with high (low) dust normalization. Dashed lines show the dust emission, dotted lines show synchrotron emission, and solid lines show the combined emission from each model. The amplitude of the combined emission is fixed at both 22 GHz and 408 MHz. Measurements below 10 GHz are dominated by synchrotron, which can be used to infer the dust normalization: models with more dust emission at 22 GHz have lower synchrotron emission. Grey bars indicate the ARCADE 2 frequency bands.

well with the thermal dust morphology) to the Haslam map at 408 MHz (observed to correlate only weakly with thermal dust emission). Model discrimination based on cross-correlations with thermal dust emission must rely on rigorous statistical comparison of competing models, and not simply on the general trend toward weaker correlations at lower frequencies.

A simpler test relies on the absolute spectrum of Galactic emission. At frequencies below 30 GHz, thermal dust emission is negligible, so that the total Galactic emission becomes a superposition of free-free, synchrotron, and spinning dust emission. Both free-free and synchrotron emission increase monotonically at lower frequencies. Spinning dust, in contrast, *decreases* in amplitude below 20 GHz, so that the spectrum of the combined Galactic emission below 20 GHz can be used to place limits on the contribution of spinning dust without reference to detailed spatial correlations with a thermal dust template.

Figure 8 illustrates the concept. Consider Galactic emission consisting of a superposition of synchrotron and spinning dust (ignoring for the moment the smaller contribution from free-free emission). Following Miville-Deschênes et al. (2008), we specify the spinning dust amplitude as a fraction of the total Galactic brightness at 22 GHz, assumed here to represent the peak in the dust spectrum. As the dust normalization is increased, the synchrotron amplitude at 22 GHz must decrease to keep the total emission constant. The spinning dust spectrum falls rapidly, so that emission below 10 GHz is dominated by the synchrotron component. A model with high dust normalization (red curves in Fig. 8) will thus have fainter synchrotron emission at frequencies of a few GHz, while a model with less spinning dust (blue curves) will have brighter synchrotron emission. This shift in the amplitude of Galactic emission at frequencies below 10 GHz is a sensitive test for spinning dust, without resort to detailed spatial correlations.

We implement this test using a simple model of Galactic emission. We assume that the spatial distribution of spinning dust emission is traced by a template map of thermal dust emission, and fix the amplitude of associated spinning dust emission by scaling the template map so that the re-scaled dust map forms a specified fraction of the Galactic plane intensity measured by the WMAP 22 GHz map. This allows a simple normalization of spinning dust in terms of its relative contribution to the total Galactic plane intensity at 22 GHz. We use the COBE/DIRBE 240 μm map of thermal dust emission (Reach et al. 1996) as the thermal dust template since it is dominated by thermal dust emission but unaffected by extinction in the plane. For specificity, we define the Galactic plane mask using all pixels lying within the ARCADE 2 observation pattern with latitude $|b| < 20^\circ$, and use this mask for all computations so that the model results are not affected by differing sky coverage between ARCADE 2 and other surveys.

We then model the Galactic emission spectrum as follows. We first correct the WMAP 22 GHz map and the Haslam 408 MHz map by subtracting the WMAP maximum-entropy model of free-free emission (Gold et al. 2008) using a spectral index $\beta_{\text{ff}} = -2.15$. The corrected maps then contain only synchrotron and (possibly) spinning dust emission. We assume that the

spinning dust spectrum peaks at 22 GHz and scale the normalized spinning dust map to lower frequencies using the Draine & Lazarian (1998) model for the warm neutral medium. After correction for free-free and spinning dust emission, the 22 GHz and 408 MHz maps contain only synchrotron emission, which we use to define the synchrotron amplitude and spectral index for each pixel.

The resulting model (synchrotron, free-free, and spinning dust) can be used to estimate the combined Galactic emission at frequencies between 408 MHz and 22 GHz. We compare the model to the ARCADE 2 data by smoothing the model map of combined emission to the ARCADE 2 angular resolution, and then computing the mean Galactic emission of the smoothed model for all pixels within the ARCADE 2 galactic plane mask. Figure 9 shows the result. If spinning dust is negligible, the synchrotron contribution at 22 GHz is maximal and the model approximates the flat-spectrum synchrotron model. As the spinning dust amplitude increases, the synchrotron contribution at 22 GHz decreases and the synchrotron spectral index steepens. The combination of lower synchrotron amplitude and falling dust spectrum combine to lower the total model emission across

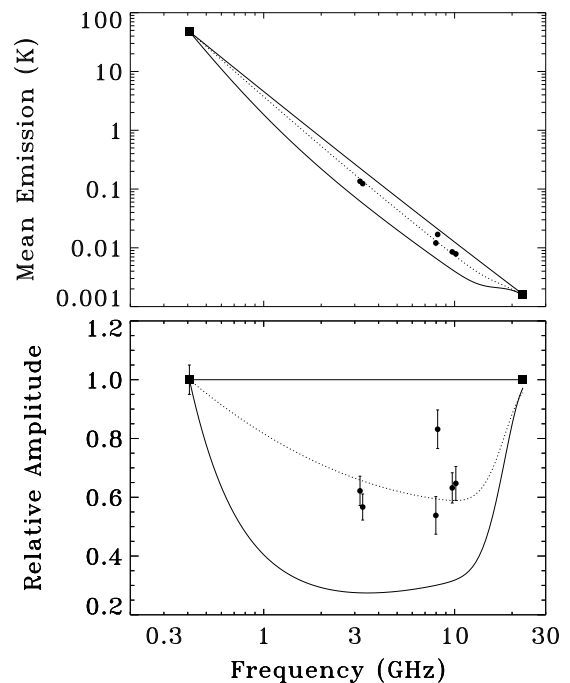


FIG. 9.— Mean intensity of Galactic plane emission for the ARCADE 2 data, compared to model predictions with and without spinning dust (see text). Top panel: Model predictions and data. The upper solid curve shows the model prediction for no spinning dust, averaged over the ARCADE 2 sky coverage with $|b| < 20^\circ$. The lower solid curve shows the model prediction for spinning dust amplitude equal to 60% of the total Galactic plane emission at 22 GHz. The dotted curve shows the best fit to the ARCADE 2 data. The spectrum of emission from spinning dust is assumed to peak at 22 GHz, so a higher spinning dust fraction at 22 GHz produces lower total emission at the ARCADE 2 frequencies. The bottom panel shows the same data, normalized by dividing each point by the model prediction for no spinning dust. Galactic plane emission observed by ARCADE 2 is consistently fainter than expected for a model with no spinning dust, and is consistent with spinning dust contributing 0.4 ± 0.1 of the total Galactic plane emission at reference frequency 22 GHz.

the ARCADE 2 frequency bands. The ARCADE 2 data lie below the model prediction for no spinning dust, and are consistent with spinning dust contributing 0.4 ± 0.1 of the total K-band Galactic plane emission.

WMAP is a differential instrument and is insensitive to any monopole emission component. The zero level of the 22 GHz map is set using the cosecant dependence on Galactic latitude (Hinshaw et al. 2008). The 408 MHz survey and the ARCADE 2 data, however, both include monopole contributions. To prevent discrepant treatment of the map zero levels from affecting the model predictions, we remove a monopole from the 408 MHz survey and the ARCADE 2 sky maps, and re-set the zero level of each map using a $\csc(|b|)$ fit to the spatial structure in each map to match the processing of the WMAP data. We restrict analysis to pixels at low Galactic latitude ($|b| < 20^\circ$) where Galactic emission is brightest so that uncertainties in the zero level have minimal effect. The largest uncertainty in the analysis is the correction for free-free emission. We use the WMAP maximum-entropy model of free-free emission, derived assuming that spinning dust contributes negligibly to the total Galactic emission. We test the sensitivity of the result to the free-free normalization by repeating the analysis using the same maximum-entropy model scaled by a constant normalization factor. Changing the free-free normalization by a factor of 2 affects the best-fit spinning dust normalization by approximately 0.08, and is included in the total quoted uncertainty.

6. CONCLUSIONS

We use the ARCADE 2 absolutely calibrated observations of the sky to model Galactic emission at frequencies 3, 8, and 10 GHz and angular resolution $11.6''$. TT plots of the binned sky maps show net spectral index $\beta = -2.43 \pm 0.03$ between 3.3 and 8.3 GHz and $\beta = -2.47 \pm 0.02$ between 3.3 and 10.3 GHz, consistent with a superposition of synchrotron and free-free emission. The spatial structure in the maps can be described using two spatial templates, the Haslam 408 MHz survey to trace synchrotron emission and the COBE/FIRAS map of CII emission to trace free-free emission. Fitting these templates to the ARCADE 2 maps yields spectral index $\beta_{\text{synch}} = -2.5 \pm 0.1$ for emission traced by the synchrotron template, with free-free normalization $\langle T_{\text{ff}}/T_{\text{total}} \rangle = 0.10 \pm 0.01$ evaluated for latitudes $|b| < 10^\circ$ in the lowest ARCADE 2 channel at 3.15 GHz.

The template model only specifies Galactic emission up to an additive constant. We fully specify the Galactic model by computing the temperature of the template model toward three reference locations (north and south polar caps plus the coldest patch in the Northern hemisphere), and adding a constant to the template model to match the Galactic temperature derived by other means. One estimate of the Galactic temperature models the Galaxy as a simple plane-parallel structure and derives the polar cap temperatures from the slope of the Galactic emission binned by the cosecant of Galactic latitude.

A second, independent method computes the correlation between radio emission and CII line emission, then estimates the radio brightness at each reference position by multiplying the CII intensity at that position by the measured radio/CII correlation slope. Both methods yield similar estimates for the total Galactic temperature towards each reference location. We extend the analysis to full-sky surveys at lower frequencies and find that Galactic polar cap temperature from both methods is consistent with a single power law over the frequency range 22 MHz to 10 GHz, with spectral index $\beta = -2.55 \pm 0.03$ and normalization 0.498 ± 0.028 K at reference frequency $\nu_0 = 1$ GHz.

ARCADE2 produces well-calibrated maps of Galactic emission. We use these maps to test for contributions from spinning dust near the Galactic plane. Previous tests for spinning dust at frequencies below 20 GHz have used only the spatial correlation with template maps tracing thermal dust emission. The frequency dependence of the dust-correlated component is not a stringent test for spinning dust, since a weaker correlation at lower frequencies is expected both for models with significant spinning dust contributions as well as models with flat-spectrum synchrotron but no spinning dust. We use a simple model of the total Galactic emission to predict the mean intensity of the Galactic plane in the region observed by ARCADE 2. The model normalizes the spinning dust contribution at 22 GHz, and computes the expected total contribution from free-free, synchrotron, and spinning dust as a function of frequency and spinning dust normalization. The ARCADE 2 data consistently show less emission in the Galactic plane than a model with no spinning dust, and are consistent with spinning dust contributing 0.4 ± 0.1 of the Galactic plane emission at 22 GHz.

We thank the staff of the Columbia Scientific Balloon Facility for their capable support throughout the integration, launch, flight, and recovery of the ARCADE 2 mission. We thank the students whose work helped make ARCADE 2 possible: Adam Bushmaker, Jane Cornett, Sarah Fixsen, Luke Lowe, and Alexander Rischard. We thank P. Reich for providing the 45 MHz and 1420 MHz surveys in electronic format. We acknowledge use of the HEALPix software package. This research is based upon work supported by the National Aeronautics and Space Administration through the Science Mission Directorate under the Astronomy and Physics Research and Analysis suborbital program. The research described in this paper was performed in part at the Jet Propulsion Laboratory, California Institute of Technology, under a contract with the National Aeronautics and Space Administration. T.V. acknowledges support from CNPq grants 466184/00-0, 305219-2004-9 and 303637/2007-2-FA, and the technical support from Luiz Reitano. C.A.W. acknowledges support from CNPq grant 307433/2004-8-FA.

REFERENCES

- Alvarez, H., Aparici, J., May, J., and Olmos, F., 1997, *A&AS*, 124, 315
 Bennett, C. L., et al., 2003, *ApJS*, 148, 97
 Dobler, G. and Finkbeiner, D. P., 2007, *ApJ*, submitted (preprint arXiv:0712.1038)
 Draine, B. T. and Lazarian, A., 1998, *ApJ*, 494, L19
 Fernández-Cerezo, S., et al., 2006, *MNRAS*, 370, 15

- Finkbeiner, D. P., 2003, *ApJS*, 146,407
Finkbeiner, D. P., Davis, M., and Schlegel, D.J., 1999, *ApJ*, 524, 867
Fixsen, D. J. et al., 2008, *ApJ*, submitted
Fixsen, D. J. et al., 2004, *ApJ*, 612, 86
Fixsen, D. J., Bennett, C. L., and Mather, J. C., 1999, *ApJ*, 526, 207
Gold, B. et al., 2008, *ApJ*, submitted (preprint arXiv:0803.0715)
Haslam, C. G. T., et al., 1981, *A&A*, 100, 209
Hildebrandt, S. R., et al., 2007, *MNRAS*, 382, 594
Hinshaw, G., et al., 2008, *ApJS*, in press (preprint arXiv:0803.0732)
Kalberla, P. M. W., et al., 2005, *A&A*, 440, 775
Kogut, A. et al., 2004, *ApJS*, 154, 493
Kogut, A., et al., 1996, *ApJ*, 460, 1
Kogut, A., et al., 1996, *ApJ*, 464, L5
Leitch, E. M., et al., 1997, *ApJ*, 486, L23
Maeda, K., Alvarez, H., Aparici, J., May, J., and Reich, P., 1999, *A&AS*, 140, 145
Miville-Deschênes, M.-A., et al., 2008, *A&A*, submitted (preprint arXiv:0802.3345)
de Oliveira-Costa, A., et al., 2004, *ApJ*, 606, L89
de Oliveira-Costa, A., et al., 1997, *ApJ*, 482, L17
Platania, P. et al., 1998, *ApJ*, 505, 473
Reach, W. T., et al., 1996, *AIP Conf Proc.* 348, 37
Reich, P., Testori, J. C., and Reich, W., 2001, *A&A*, 376, 861
Reich, P., and Reich, W., 1986, *A&AS*, 63, 205
Roger, R. S., Costain, C. H., Landecker, T. L., and Swerdlyk, C. M., 1999, *A&AS*, 137, 7
Rogers, A. E. & Bowman, J. D. 2008, *AJ*, in press (preprint arXiv:0806.2868)
Rybicki, G. B. & Lightman, A. 1979, *Radiative Processes in Astrophysics* (Wiley & Sons: New York)
Seiffert, M. et al., 2008, *ApJ*, submitted
Singal, J. et al., 2008, *ApJ*, submitted
Singal, J. et al., 2006, *ApJ*, 653, 835
Singal, J. et al., 2005, *Rev. Sci. Inst.*, 76, 124073
Tartari, A., et al., 2008, *ApJ*, in press (preprint arXiv:0806.4306)